https://doi.org/10.5194/gmd-2023-196
Preprint. Discussion started: 2 November 2023

Geoscientific Model Development Discussions

Open Boundary Conditions for Atmospheric Large Eddy Simulations and the Implementation in DALES4.4

Franciscus Liqui Lung[1], Christian Jakob[1], A. Pier Siebesma[2,3], and Fredrik Jansson[2]

[1]Monash University, Melbourne, Victoria, Australia
[2]Delft University of Technology, Delft, The Netherlands
[3]The Royal Netherlands Meteorological Institute, De Bilt, The Netherlands

Correspondence: Franciscus Liqui Lung (franciscus.liquilung@monash.edu)

Abstract. Open boundary conditions were developed for atmospheric large eddy simulation (LES) models and implemented into the Dutch Atmospheric Large Eddy simulation model. The implementation was tested in a "Big Brother"-like setup, in which the simulation with open boundary conditions was forced by an identical control simulation with periodic boundary conditions. The results show that the open boundary implementation has minimal influence on the solution. Both the mean state and the turbulent structures are close to the control simulation and disturbances at the in- and outflow boundaries are negligible. To emulate a setup in which the LES is coupled to a coarser model, the influence of coarse boundary input was tested by smoothing the output of the periodic control simulation both temporally and spatially before feeding it as input to the simulation with open boundary conditions. The results show that when the ratio between input and model resolution increases, disturbances start to form at the inflow boundary and an area exists where turbulence needs to develop. Adding synthetic turbulence to the smoothed input reduces the size of this area and the magnitude of the disturbances.

1 Introduction

Large eddy simulation (LES) is a numerical simulation tool used to study small scale weather phenomena in the atmospheric boundary layer (ABL). Employing resolutions ranging from $1 - 100\mathrm{m}$, the largest turbulent eddies containing most turbulent kinetic energy (TKE) are resolved, whereas the effects of smaller unresolved eddies are parameterised. With most of the TKE being resolved, LES has the advantage over coarser limited area models (LAMs) when it comes to representing the effects of boundary layer turbulence. This advantage comes at the cost of domain size and/or simulation time. Idealised ABL studies using LES started in the late sixties/early seventies (e.g. Lilly, 1966; Deardorff, 1972; Sommeria, 1976). Traditionally, LES was mainly used to study ABLs with idealized homogeneous forcings, employing periodic lateral boundary conditions (LBCs).

With the increase in computational power, the use of LES has shifted from idealised cases to more complex and realistic scenarios. Some examples are the simulation of urban areas (e.g. Giometto et al., 2016; Kurppa et al., 2018), windfarms (e.g. Mehta et al., 2014) and very large case studies pushing towards domain sizes of $\mathcal{O}(1000\mathrm{km})$ (e.g. Schalkwijk et al., 2015; Heinze et al., 2017). For the latter it is especially important to capture the heterogeneity present in the domain. Periodic LBCs are by definition not suited for this (Moeng et al., 2007). Furthermore, it is often desired to couple LES to a regional weather model to transfer large-scale atmospheric structures. For these reasons, it is desirable to have open LBCs in place. Ideally,

https://doi.org/10.5194/gmd-2023-196
Preprint. Discussion started: 2 November 2023


Geoscientific Model Development Discussions

open LBCs allow the prescription of fields at inflow boundaries and propagate fields unperturbed out of the domain at outflow boundaries.

There is no consensus on the "best" implementation of open boundary conditions for anelastic turbulent flow. In 1991 two mini-symposia were unsuccessfully dedicated to this topic and the effort was summarized as a frustrating one (Sani and Gresho, 1994). A popular choice is an outflow condition based on the radiation condition of Sommerfeld (1949). The radiation BC states that waves generated in the interior of the domain should propagate outwards with no reflections at the boundaries. It takes the form of a propagating wave and replaces the Navier-Stokes equations at the boundaries. The difficulty lies in determining the phase speed of the wave, which is required for applying the radiation boundary condition. Different implementations for the phase speed have been defined (e.g. Orlanski, 1976; Klemp and Wilhelmson, 1978; Hedley and Yau, 1988). Orlanski (1976) uses a variable phase speed that is defined upwind of the boundary and propagated to the boundary. The results of a 2D test case show that the implementation works well and results in minimal reflections. Klemp and Wilhelmson (1978) use radiation LBCs in their 3D storm model and evaluate their influence in a 2D version of the model. They define their phase speed as a constant plus the local boundary-normal velocity component. Using a similar test setup as Orlanski (1976), Klemp and Wilhelmson (1978) show that their implementation is capable of producing realistic results. They do note that the results are sensitive to the choice of the fixed part of the phase speed. Hedley and Yau (1988) compare the implementations of Orlanski (1976) and Klemp and Wilhelmson (1978) with their new implementation that is a hybrid version of the implementation of Orlanski (1976). They conclude that their hybrid implementation is superior to both. Craske and Van Reeuwijk (2013) give a summary of open BCs for incompressible turbulent flows and state that a radiation outflow condition results in the least amount of distortion for convection dominated flows. Incompressible LES models such as PALM (Maronga et al., 2020) and MESO-NH (Lac et al., 2018) and the fully compressible WRF-LES (Skamarock et al., 2021) have the option to use radiation boundary conditions for the boundary-normal velocity components based on one of the previously mentioned implementations. For the other variables (homogeneous) Neuman BCs are often used at outflow boundaries, which specify the boundary-normal derivative. For inflow conditions Dirichlet(-like) boundary conditions are common, which specify the fields at the boundary.

The implementation of open LBCs make it possible to nest LES within both itself and mesoscale models (e.g. Moeng et al., 2007; Zhu et al., 2010; Talbot et al., 2012; Mazzaro et al., 2017; Heinze et al., 2017; Kadasch et al., 2021). These studies used prescribed boundary conditions instead of radiation BCs to nest their LES. Prescribed boundary conditions are a Dirichlet boundary condition, where the LBCs of the child simulation are directly prescribed by the mother simulation. These type of prescribed LBCs are similar to what is used in the mesoscale modelling community and are intuitive to implement. Dirichlet boundary conditions are however known to create reflections and a numerical boundary layer at outflow boundaries for turbulent flows (e.g. Wesseling, 2009; Ol'shanskii and Staroverov, 2000). The prescribed boundary condition is therefore often accompanied with a relaxation zone (Moeng et al., 2007; Zhu et al., 2010; Heinze et al., 2017), in which the fields near the boundary are nudged towards the boundary values to dampen any numerical noise due to the LBCs. Moeng et al. (2007) use WRF-LES to conduct two-way nested simulations of LES nested within LES. They conclude that the nesting works well for LES within LES but state the challenges that will arise for both one-way and two-way nesting of LES within a mesoscale model. Mesoscale models will have different vertical profiles due to their turbulent transport parametrisations in the PBL as opposed to

https://doi.org/10.5194/gmd-2023-196
Preprint. Discussion started: 2 November 2023


Geoscientific Model Development Discussions
Open Access
EGU

the 3D resolved turbulence of LES. Furthermore, since mesoscale models are non-turbulence resolving, the lack of turbulence at inflow boundaries will result in a spinup area required for turbulence to develop. The spinup area is further increased by the implementation of a relaxation zone, as it does not only dampen numerical artifacts but turbulence as well. Zhu et al. (2010) tested both a one-way and two-way nested setup with WRF-LES being forced by National Centers for Environmental Prediction (NCEP) reanalysis data. They found that the relaxation zone in the outermost model is able to mitigate potential problems with the large resolution jump between the coarsest WRF-LES domain and the NCEP data set. However, they found that the cloud fields can be strongly modulated by mesoscale organisation, especially in high wind conditions where the clouds align with the mean wind direction. They found little benefit of two-way nesting over one-way nesting. Talbot et al. (2012) coupled WRF-LES within WRF in a realistic one-way nesting setup using 3 LES domains with increasing resolution in 3 mesoscale domains. They found that the use of a nested LES setup mainly improves the surface fluxes and near surface fields, but the bulk ABL dynamics such as boundary layer height of the mesoscale models agreed better with observations. They also found that the initial and boundary forcings were most important for the results and had a much bigger influence than the choice of subgrid scheme. Mazzaro et al. (2017) studied the effect of unresolved mesoscale flows on LES. They forced three similar LES domains with different resolution mesoscale simulations. They test their results both with and without the addition of the cell perturbation method of Muñoz-Esparza et al. (2014, 2015) and find that the LES is capable to overcome erroneous features in the mesoscale output. The cell perturbation scheme helps to greatly reduce the distance required for turbulence to develop, especially for the coarser mesoscale forcings. The best results are obtained with the highest resolution mesoscale model. Heinze et al. (2017) used a one-way nesting approach to employ realistic LES over Germany. Three domains were used to step down from 625m horizontal resolution to 156m with a constant grid refinement factor of two. They compared their results to the observations of the HD(CP^2) campaign and conclude that when it comes to small-to-mesoscale variablity the use of LES drastically improves the results compared to their reference mesoscale model COSMO. PALM has also recently implemented an option for offline nesting within COSMO (Kadasch et al., 2021). They employ prescribed boundary conditions and impose synthetic turbulence in addition to the boundary fields. At the moment there is no relaxation zone implemented, but they do note that this might change in the future. In their test cases, they find that the boundary input has the largest impact on the main flow structures. Flow and updrafts rapidly develop with the help of the synthetic turbulence routine. Fully developed turbulence was found after two to three times the distance corresponding to the eddy turnover time.

In this research we develop a set of open LBCs for anelastic LES and implement it in the Dutch Atmospheric Large Eddy Simulation model (DALES). The goal of the paper is threefold. First, we will give a clear and extensive description of the open LBCs developed in this research. Second, we will show the influence of the LBCs on the mean fields and turbulent characteristics. Third, we will see how the results depend on the temporal and spatial resolution of the input data, emulating a setup where the LES is coupled to a coarser, non-turbulence resolving, LAM. The LBCs are developed to minimize reflections and the area needed for turbulence to develop and to allow for one-way nesting with coarser LAMs. To minimise reflections, the outflow boundary conditions will be based on the radiation boundary condition of Sommerfeld (1949) and for the inflow boundary a new set of Robin boundary conditions will be derived. To allow for one-way coupling with coarser LAMs, the open LBCs will be developed such that they allow time varying input. The LBCs are tested with a simplistic dry convective case in

https://doi.org/10.5194/gmd-2023-196
Preprint. Discussion started: 2 November 2023

Geoscientific Model Development Discussions

a "big-brother" like setup (Denis et al., 2002). This allows us to single out the influence that the LBCs have on the fields in the interior of the domain. To study the influence of the spatial and temporal resolution of the boundary input data, the turbulence in the input data is filtered both in space and time simultaneously. This allows us to study the influence of the open LBCs in a setup where the LES is coupled to a non-turbulence resolving model and quantify the influence of the spatial and temporal resolution ratios between the mother and child model. We will investigate how long it takes for turbulence to fully develop. Furthermore, the influence of synthetic turbulence on generating inflow turbulence is explored.

2 Boundary condition implementation

This section will describe the implementation of the open boundary conditions in the Dutch Atmospheric Large Eddy Simulation (DALES) model (Heus et al., 2010). The presented open boundary implementation is applicable to any incompressible atmospheric LES and except for the discussion about mass conservation, could also be used for fully compressible LES. DALES solves the anelastic Navier-Stokes equations on a staggered Arakawa-C grid. The prognostic variables are the three velocity components (u, v, w), liquid potential temperature (θ_l), total water specific humidity (q_t), the rain water specific humidity (q_r), the rain droplet number concentration (N_r), the subfilter scale turbulence kinetic energy (e) and up to 100 active or passive scalars. Appropriate boundary conditions are required for all the prognostic variables. The velocity components are located at their respective cell faces and the rest of the variables at the cell centres. The boundary is defined as the cell faces of the outermost grid cells. Therefore, the boundary-normal velocity components are located at the boundary, whereas the other variables are located offset from the boundary. First, the implementation for the boundary-normal velocity components will be given and conservation of mass will be discussed. Second, the implementation for the other variables is described. Third, the algorithm used to add synthetic turbulence at the boundaries will be discussed.

2.1 Boundary-normal velocity components

The boundary condition for the boundary-normal velocity components depends on whether the cell is an in- or outflow cell. An inflow cell for the boundary-normal velocity component is defined as $\mathbf{u}^B \cdot \hat{n} < 0$, where $\mathbf{u}^B$ is the input velocity vector specified at the boundary, given by external data, and $\hat{n}$ the outward pointing boundary normal unit vector. An outflow cell is defined by $\mathbf{u}^B \cdot \hat{n} \geq 0$.

2.1.1 Outflow

The outflow boundary condition is based on the Sommerfeld radiation boundary condition (Sommerfeld, 1949), which states that disturbances should only be advected out of the domain with no reflections. The radiation boundary condition takes the form of a single propagating wave.

$$\frac{\partial u_n}{\partial t} = -\frac{U}{\rho}\frac{\partial \rho u_n}{\partial n} + \left(g\frac{\theta - \langle\theta\rangle}{\langle\theta\rangle}\right)\hat{z} + \epsilon \tag{1}$$

https://doi.org/10.5194/gmd-2023-196
Preprint. Discussion started: 2 November 2023


Geoscientific Model Development Discussions
Open Access
EGU

In Eq. (1) u_n is the boundary-normal velocity component, U the advection/phase speed of the disturbances, $\partial/\partial n$ the boundary-normal derivative, ρ the reference density profile used by DALES, $\hat{z}$ the unit vector in the vertical direction, θ the potential temperature, g the gravitational acceleration, ϵ a correction factor required to conserve mass, which will be explained in more detail in Sect. 2.1.3 and $\langle\rangle$ denotes a horizontal slab average. For the vertical component the buoyancy force is added which works as a damping factor for the top boundary in stably stratified flows. For non-dispersive waves with a phase speed equal to U, Eq. (1) will not generate any reflections. In the case of atmospheric simulations, which is a dispersive system, the transport velocity U needs to be chosen carefully, such that reflections are minimised. Popular implementations for the phase speed are given by Orlanski (1976) used by PALM (Maronga et al., 2015, 2020) and by Klemp and Wilhelmson (1978) used in MESO-NH (Lafore et al., 1998; Lac et al., 2018) and WRF-LES (Skamarock et al., 2021). Here we will use a slightly adjusted version of the implementation given by Hedley and Yau (1988). The implementation of Hedley and Yau (1988) is a hybrid version of the implementation given by Orlanski (1976) and is shown to work better. Similar to Orlanski (1976), the velocity field and tendencies upstream of the boundary at the previous time step are used to define the local phase speed, which is then propagated to the boundary for the next time step. Additionally, Hedley and Yau (1988) set a fixed lower limit for the phase speed. We will set the lower limit to the boundary input normal velocity component, u_n^B.

$$U = U|^{t-\Delta t}_{x_n - \hat{x}\cdot\hat{n}\Delta x_n} = \left\langle -\rho \frac{\partial u_n}{\partial t} \left(\frac{\partial \rho u_n}{\partial n} \right)^{-1} \right\rangle^{\text{int}}$$
$$\left|u_n^B\right| \leq |U| \leq \frac{\Delta x_n}{\Delta t} \tag{2}$$

In Eq. (2) $t-\Delta t$ denotes the previous time step and $x_n - \hat{x}\cdot\hat{n}\Delta x_n$ the grid cell directly upstream of the boundary. To avoid large fluctuations in the phase speed due to local gradients, the phase speed is averaged over the horizontal dimensions perpendicular to the boundary vector over a distance of Δx^{int} and Δy^{int}, denoted by $< >^{\text{int}}$. This is similar to PALM, which averages laterally over the entire boundary (Maronga et al., 2015). For stability reasons the upper bound of the phase velocity is set to the CFL condition. Equation (2) is discretised using a second order forward scheme.

2.1.2 Inflow

For inflow cells a Dirichlet boundary condition is used for the boundary-normal velocity components. The Dirichlet condition is implemented as a tendency to work well with the pressure solver used in DALES.

$$\frac{\partial u_n}{\partial t} = \frac{u_n^B - u_n}{\Delta t} + \epsilon, \tag{3}$$

In Eq. (3) Δt is the integration time step of DALES.

2.1.3 Conservation of mass

The use of radiation boundary conditions means that continuity is not guaranteed and a correction factor, ϵ needs to be added. Hedley and Yau (1988) enforce that the height integrated mass flux through each boundary does not change in time. This limits

https://doi.org/10.5194/gmd-2023-196
Preprint. Discussion started: 2 November 2023

Geoscientific Model Development Discussions

however the functionality for time-varying wind fields, in which inflow boundaries can become outflow boundaries and vice versa. Here we derive a correction term that forces the mass flux through the boundary to the boundary input on a defined length scale. This allows the wind field to change in magnitude and direction over time. To conserve mass the following constrains are imposed.

1. The input boundary-normal velocity components satisfy the continuity equation conform to the reference density profile used by DALES,

$$\oiint_{S(B)} \rho \mathbf{u}^B \cdot \hat{n} \, \mathrm{d}S = 0 \tag{4}$$

2. On boundary patches defined by $\Delta x^{\text{int}}, \Delta y^{\text{int}}, \Delta z$, the integrated mass flux equals the integrated mass flux given by the input velocities.

$$\iint_{S^{\text{int}}} \rho \mathbf{u} \cdot \hat{n} \, \mathrm{d}S = \iint_{S^{\text{int}}} \rho \mathbf{u}^B \cdot \hat{n} \, \mathrm{d}S \tag{5}$$

To obtain the correction factor ϵ, we define ϵ to be piecewise continuous on the integration patches. Taking the time derivative of Eq. (5) gives us then an expression for ϵ.

$$\epsilon\left(S^{\text{int}}\right) = \frac{\iint_{S^{\text{int}}} \rho \left(\frac{\partial u_n^B}{\partial t} - \frac{\partial \tilde{u}_n}{\partial t} \right) \mathrm{d}S}{\iint_{S^{\text{int}}} \rho \, \mathrm{d}S} \tag{6}$$

In Eq. (6) $\frac{\partial \tilde{u}_n}{\partial t} = \frac{\partial u_n}{\partial t} - \epsilon$, is the tendency at the boundary without the correction factor. ϵ can be physically interpreted as the correction required to force the mass flux through the integration area S^{int} to the mass flux as given by the input. Within one integration patch the mean of the boundary-normal mass flux is forced to the mean of the input mass flux, while the smaller scale perturbations are preserved. Dirichlet conditions are obtained when the integration length scales are set equal to the DALES resolution.

Since the role of the pressure term in the anelastic approximation is to conserve mass, one can interpret the correction term as a pressure boundary condition. It is possible to use a non-homogeneous Neumann condition for the pressure solver such that the resulting tendency corresponds to the correction term. However, we choose to add the term in the equations for the boundary-normal velocity components and use homogeneous Neumann boundary conditions for the pressure field. This allows us to keep using the Fourier pressure solver, by using cosine basis functions only.

At the moment the vertical length scale of the integration patch is fixed to the vertical grid resolution. This allows for a straightforward implementation when using stretched vertical grids. We have also experimented with setting the vertical length scale of the integration patch to the domain height. This couples the boundary layer with the column above the inversion layer and gave unwanted results. In the future the implementation can be extended to allow for a variable vertical integration length scale as well.

https://doi.org/10.5194/gmd-2023-196
Preprint. Discussion started: 2 November 2023

Geoscientific Model Development Discussions

2.2 Cell-centered variables

This section will discuss the boundary conditions for the cell-centered variables and the tangential velocity components. These variables are not computed at the boundary. Instead, ghost cells are used together with a second order central discretisation to determine the behaviour of the variable at the boundary. The implementation is different for in- and outflow boundaries. For the cell-centered variables and tangential velocity components, a boundary is defined as inflow if $\mathbf{u} \cdot \hat{n} < 0$ and as outflow otherwise. Note that this is different from the definition for the boundary-normal velocity components, where the nature of the boundary is determined by the input velocity u_n^B. These two can differ for outflow boundaries when the advection velocity is low and turbulence strong enough to reverse the local flow direction, as the radiation boundary condition does not enforce outflow on the local scale.

2.2.1 Outflow

For outflow cells homogeneous Neumann conditions, Eq. (7), are specified at the lateral boundaries.

$$\frac{\partial \psi}{\partial n} = 0 \tag{7}$$

In Eq. (7) ψ is any of the cell centered variables (θ_l, q_t, q_r, N_r, e) or tangential velocity components. At the top of the domain Neumann boundary conditions are set, which take the slab averaged vertical derivative into account,

$$\frac{\partial \psi}{\partial z} = \frac{\partial \langle \psi \rangle}{\partial z} \tag{8}$$

in which <> denotes a slab average. Neumann conditions work well for outflow boundary conditions because conditions on the derivative result in a weaker numerical boundary layer compared to conditions set on the function itself (Sani and Gresho, 1994).

2.2.2 Inflow

For inflow boundaries, Dirichlet boundary conditions are a common choice (e.g. Maronga et al., 2015; Lac et al., 2018). However, for flows in which boundary cells frequently change between in -and outflow boundaries, such as turbulent flows, Dirichlet boundary conditions can give large gradients over the boundaries which result in extreme tendencies. MESO-NH poses a less strict Dirichlet inflow boundary condition by setting the boundary value to a weighted average between the input value and the nearest LES domain value, with a weight of 0.8 for the interior values (Lac et al., 2018). In this research we take a different approach and implement a Robin boundary condition, which will be derived in this section. The Robin boundary condition is a weighted average between a Dirichlet and Neumann boundary condition.

We impose that advection over an inflow boundary nudges the boundary value to a given input value ψ^B within a given time scale τ. The tendency at the boundary can be written as:

$$\frac{\partial \psi}{\partial t} = -u_n \frac{\partial \psi}{\partial n} = \frac{\psi^B - \psi}{\tau} \tag{9}$$

https://doi.org/10.5194/gmd-2023-196
Preprint. Discussion started: 2 November 2023

Geoscientific Model Development Discussions

Equation (9) can be rewritten in the form of a Robin boundary condition.

$$\psi - u_n \tau \frac{\partial \psi}{\partial n} = \psi^B \tag{10}$$

The behaviour of Eq. (10) is determined by the value of $u_n\tau$. Dirichlet and homogeneous Neumann conditions correspond to different limits.

$$\lim_{u_n\tau \to 0} \psi = \psi^B \text{ (Dirichlet)}$$
$$\lim_{u_n\tau \to \pm\infty} \frac{\partial \psi}{\partial n} = 0 \text{ (Homogeneous Neumann)} \tag{11}$$

The classical Dirichlet inflow conditions can thus be obtained by setting $\tau = 0$. When $\tau \neq 0$ the boundary condition transitions from Dirichlet to homogeneous Neumann conditions as the velocity increases, avoiding large fluxes into the domain. At $u_n = 0$ the transition point between in- and outflow conditions, the boundary condition changes from Dirichlet (inflow), $u_n\tau = 0$, to homogeneous Neumann (outflow). This transition can be smoothed by introducing a variable timescale for the inflow conditions. The inflow conditions were derived with the proposition that advection nudges the boundary over a fixed time scale. At very low velocities advection plays a minor role and this assumption breaks down. To overcome this, the time scale needs to increase as the velocity approaches 0. The following requirements are set for τ:

$$\lim_{u_n \to 0} u_n \tau = \infty$$
$$\lim_{u_n \to \infty} \tau = \tau_0$$
$$\tau_0 = 0 \Rightarrow \tau = 0 \tag{12}$$

The first condition is set such that Eq. (10) approaches homogeneous Neumann conditions for $u_n = 0$, which removes the discontinuity. The second condition specifies that for large advection velocities we would like to have a constant nudging time scale τ_0. The third condition allows to set the Robin inflow condition to Dirichlet inflow conditions when the nudging time scale is set to $\tau_0 = 0$. A dependency of $\tau \sim (1/u_n)^p$, where $p \geq 2$ satisfies the conditions. The relation used is given by:

$$\tau = \tau_0 \left[1 + \left| \frac{e}{u_n} \right|^p \right] \tag{13}$$

in which e is the subgrid velocity at the boundary. For DALES this can be taken from the TKE subgrid scheme when used. Otherwise an estimate needs to be supplied. When the resolved velocity is larger than the subgrid velocity, $u_n \gg e$, the timescale reduces to $\tau = \tau_0$. When the resolved velocity drops below the subgrid velocity the time scale will increase, providing a transition from the Robin boundary condition to the homogeneous Neumann condition at $u_n = 0$. The final form of the Robin inflow boundary conditions are given by:

$$\psi - u_n \tau_0 \left[1 + \left| \frac{e}{u_n} \right|^p \right] \frac{\partial \psi}{\partial n} = \psi^B \tag{14}$$

At the top of the domain the slab-averaged vertical gradient is taken into account. The Robin boundary condition at the top of the domain is given by:

$$\psi - w \tau_0 \left[1 + \left| \frac{e}{w} \right|^p \right] \left(\frac{\partial \psi}{\partial z} - \frac{\partial \langle \psi \rangle}{\partial z} \right) = \psi^B \tag{15}$$

https://doi.org/10.5194/gmd-2023-196
Preprint. Discussion started: 2 November 2023

Geoscientific Model Development Discussions

2.3 Synthetic turbulence routine

To investigate the potential of synthetic turbulence in reducing the turbulence spinup area, the Random Flow Generation (RFG) algorithm of Smirnov et al. (2001) is implemented. When used, ψ^B in Eq. (15) and Eq. (14) and u_n^B in Eq. (3) are replaced by $\psi^B + \psi^R$ and $u_n^B + u_n^R$ respectively, where the superscript R denotes the perturbation given by the RFG algorithm. In the calculations for the mass conservation correction factor, ϵ Eq. (6), u_n^B is still used to satisfy condition Eq. (4). The RFG algorithm involves scaling and orthogonal transformation to create non-homogeneous anisotropic (near) divergence free velocity perturbations for a given covariance matrix $\overline{u_i' u_j'}$, turbulent length scale λ and turbulent time scale τ^R from the summation of N harmonic functions. The RFG routine is extended to give correlated potential temperature perturbations as well. From experience it is known that potential temperature perturbations are more effective in initiating turbulence than momentum perturbations. To create the potential temperature perturbations, a perturbation field is created from the summation of N harmonics,

$$\begin{aligned}
&\alpha = \sqrt{\frac{2}{N}} \sum_{i=1}^{N} p_i \cos\left(\mathbf{k_i} \cdot \frac{\mathbf{x}}{\lambda} + \omega_i \frac{t}{\tau^R}\right) + q_i \sin\left(\mathbf{k_i} \cdot \frac{\mathbf{x}}{\lambda} + \omega_i \frac{t}{\tau^R}\right), \\
&p, q, \omega \in N(0,1), \\
&\mathbf{k} \in N(0, 0.5),
\end{aligned} \tag{16}$$

where $\mathbf{x}$ is the position vector, t the time and $N(\mu, \sigma)$ samples from a normal distribution with mean μ and standard deviation σ. Next, the perturbation field is scaled for a given $\overline{\theta'^2}$ and correlated to w^R for a given $\overline{w'\theta'}$.

$$\begin{aligned}
&\theta^R = \left(\rho \frac{w^R}{\sqrt{\overline{w'^2}}} + \alpha\sqrt{1-\rho^2}\right)\sqrt{\overline{\theta'^2}}, \\
&\rho = \frac{\overline{w'\theta'}}{\sqrt{\overline{\theta'^2}\,\overline{w'^2}}}
\end{aligned} \tag{17}$$

The RFG algorithm is easy to implement and is computationally inexpensive. A downside of the RFG algorithm is that it produces a Gaussian-model-like power spectrum. Huang et al. (2010) developed an improved algorithm that allows for any power spectra, but it comes with an additional computational cost. There are many other techniques and routines that are being used to help generate turbulence at inflow boundaries. However, the aim of this paper is not to study the performance of different inflow turbulence routines, but to rather show the potential of adding perturbations to the boundary input fields in general.

3 Simulation set up and methodology

The test case setup used in this research is summarized in Fig. 1 and consists of a "Big Brother"-like setup (Denis et al., 2002) to test the performance of the open LBC implementation, simulations with spatially and temporally smoothed input to test the influence of turbulence present in the input data and simulations with added synthetic turbulence in addition to

https://doi.org/10.5194/gmd-2023-196
Preprint. Discussion started: 2 November 2023

Geoscientific Model Development Discussions

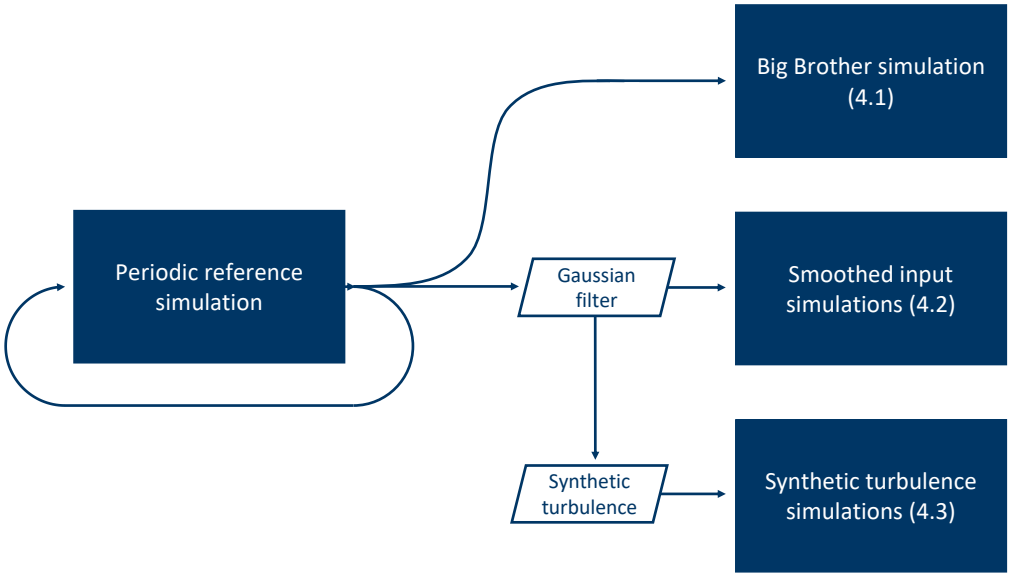

Figure 1. Illustration of the simulation setup. The solid blue rectangles show the different simulations and the sections in which their results are analyzed.

the smoothed input to see how these algorithms can help generate turbulence. The simulation case used in the test setup is the development of a dry convective boundary layer. This case is well understood and DALES is known to produce realistic results (Heus et al., 2010). Different cases such as a cloudy boundary layer and a neutral boundary layer have also been tested, but are not shown here as they show similar performance in the open LBCs. The dry convective boundary layer is forced with a constant surface heat flux that corresponds to a convective velocity scale of $w^* = 1.5\mathrm{ms}^{-1}$. The simulations are initialized with a mean advection velocity of $U = 3\mathrm{ms}^{-1}$ and a boundary layer height of $z_i = 900\mathrm{m}$. The domain size is $L_x \times L_y \times L_z = 15.36 \times 3.84 \times 1.92\mathrm{km}$ with a horizontal resolution of $\Delta x = \Delta y = 60\mathrm{m}$ and a vertical resolution of $\Delta z = 20\mathrm{m}$. The simulations last 6 hours and have an integration time step of $\Delta t = 5\mathrm{s}$. The subgrid scheme used is the SFS-TKE scheme described in Heus et al. (2010).

The "Big-Brother"-like experiment, as was first proposed by Denis et al. (2002), consists of a simulation with open boundary conditions that is directly coupled to an identical reference simulation with periodic boundary conditions. The boundary fields of the periodic simulation are communicated every time step to the simulation with open boundaries. This allows us to directly study the influence of the open boundary implementation, since both the periodic and open boundary simulation are now identically forced and only differ in the implementation of their boundary conditions. First, we carry out a sensitivity analysis to study the dependence of the solution on the parameters introduced in the open boundary implementation. The parameters will be individually perturbed around a reference set. Next, a more in depth analysis is conducted on the results of the simulation with the reference parameters. The parameters for the sensitivity analysis are listed in Table 1 with the default parameters highlighted in green.

https://doi.org/10.5194/gmd-2023-196
Preprint. Discussion started: 2 November 2023

Geoscientific Model Development Discussions
Open Access
EGU

Table 1. Settings of the open boundary implementation for the sensitivity runs. The default settings are highlighted in green.

$\Delta x_{\text{int}}/y_{\text{int}}$ (m)	p (−)	τ_0 (s)	Buoyancy term top boundary
$\Delta x/y$, $0.5L_{x/y}$, $L_{x/y}$	2, 3, 4	0, 20, 60	on, off

In practice, the open boundary conditions will often be used to couple the LES to a coarser resolution model, such as a meso-scale weather model. To study the impact of coarse resolution (in space and time) boundary conditions, the periodic output is smoothed with a Gaussian filter before it is used to force the open boundary simulation. The simulation with open boundary conditions is repeated for different degrees of spatial and temporal smoothing. This setup emulates a one-way nesting setup and moves from the LES being nested in a turbulence-resolving model to a non-turbulence-resolving model. It also allows us to study the influence of resolution ratios between mother and child model in a nested setup for both the spatial and temporal resolutions. Since the smoothed fields come from the same model with the same model physics, resolution and subgrid parametrisations, any differences between the results of the simulation with the smoothed input and the reference (periodic) simulation must be caused by the boundary implementation and the smoothing. Comparison to the case without smoothing allows us to see the influence of smoothing, which relates to the resolution/turbulent scales present in the emulated mother model.

Different techniques exist to artificially add turbulence or increase the turbulent scales present in coarse data. To demonstrate the potential of one such technique, the synthetic turbulence algorithm of Smirnov et al. (2001) is implemented and expanded to give perturbations for the potential temperature as well (Sect. 2.3). The smoothed-input open boundary simulations are repeated with the addition of synthetic turbulence. The perturbations are created using height-depended covariance matrices for $\mathbf{u}$ and θ obtained from the differences between the smoothed and non-smoothed input fields. The turbulent length scale is set to the boundary layer height, which represents the largest turbulent eddies. The turbulent time scale is calculated as the turbulent length scale over the mean advection velocity. The covariance information would not be available in a real case setup, but it allows us to see how the algorithm would perform in a best case scenario. The purpose of these simulations is not to find the best synthetic turbulence implementation, nor to fine tune the implementation used, but to give an impression on how these routines can potentially improve the results.

4 Results and Discussion

This section will describe the results of the test case described in Sect. 3. First, the performance of the open boundary implementation is evaluated using the coupled periodic/open boundary simulations. Second, the influence of input turbulence scales is described using the smoothed-input simulations. Third, the prospects of synthetic turbulence are explored.

https://doi.org/10.5194/gmd-2023-196
Preprint. Discussion started: 2 November 2023


Geoscientific Model Development Discussions

4.1 Big Brother simulation

In this section the results of the "Big Brother" experiment are shown. In this setup the periodic boundary output is given to the simulation with open boundary conditions at the same spatial and temporal resolution. To investigate the sensitivity of the solution on the parameters of the open boundary implementation, the simulation is repeated for different sets of parameters. Each of the parameters is individually perturbed around the default values. The parameters and their values are shown in Table 1. Figure 2 shows the slab average profiles calculated over the last half hour of the simulation as a perturbation from the periodic profiles for potential temperature, eastward velocity, vertical potential temperature flux and eastward velocity variance. The black line represents the solution for the default values. Each color represent a simulation where one of the parameters is perturbed and the dashed or dotted line the perturbation value. Within the boundary layer, below $1000\mathrm{m}$, the solution does not significantly depend on the values chosen for the parameters. All simulations are very close to the periodic simulation, indicating that the open boundary implementation does not have a significant impact on the solution.

At and above the inversion height the simulation with a larger timescale for the Robin inflow conditions, $\tau_0 = 60\mathrm{s}$, and the simulation without the buoyancy term in the top radiation boundary condition perform significantly worse then the other simulations. Without the buoyancy term in the top radiation boundary conditions, reflections from the top boundary result in distortions in the top layer of the simulation. Sometimes a sponge layer is implemented to dampen these type of reflections, but we don't need it here as, when used, the buoyancy term in the top radiation boundary condition solves the problem. The longer time scale for the Robin inflow conditions corresponds to a Robin boundary condition that is more weighted towards a Neumann boundary condition. A too long time scale gives too much freedom at the inflow boundary and allows for waves to build up around the inversion layer. A shorter timescale such as used in the default settings therefore works better. The default timescale is not set to zero, which corresponds to Dirichlet conditions, because a slightly relaxed condition works better for simulations with lower mean background wind speeds.

For the integration length scale Δx_{int} and Δy_{int} the simulation where they are set to the grid resolution shows the best results. This corresponds to Dirichlet boundary conditions for the boundary-normal velocity components. These settings work well for this setup, because the boundary input is turbulent, at the same resolution and from the same model. In other words, the simulation with open boundary conditions can find a solution that fits these boundary conditions. A larger integration length scale gives the LES more freedom and works better when the boundary input does not contain turbulence or is from a different model. All the results shown from here on are obtained with the default settings.

Figure 3 shows a top view of the potential temperature perturbation with respect to the periodic slab average. The cross-sections are a snapshot after 6 hours of simulation time at $110\mathrm{m}$ height. The top panel shows the results for the periodic simulation and the bottom panel for the simulation with open boundary conditions. The results of the open boundary simulation are very similar to the periodic simulation. The spatial scales and magnitude of the turbulent features resemble those of the periodic simulation. Up to $3\mathrm{km}$ from the inflow boundary (left) the turbulent features of the open boundary simulation are almost identical in shape and location to the periodic simulation, which shows that the turbulent boundary input fields at the inflow boundary are communicated well to the open boundary simulation. Further downwind they start to deviate as a result of

https://doi.org/10.5194/gmd-2023-196
Preprint. Discussion started: 2 November 2023

Geoscientific Model Development Discussions

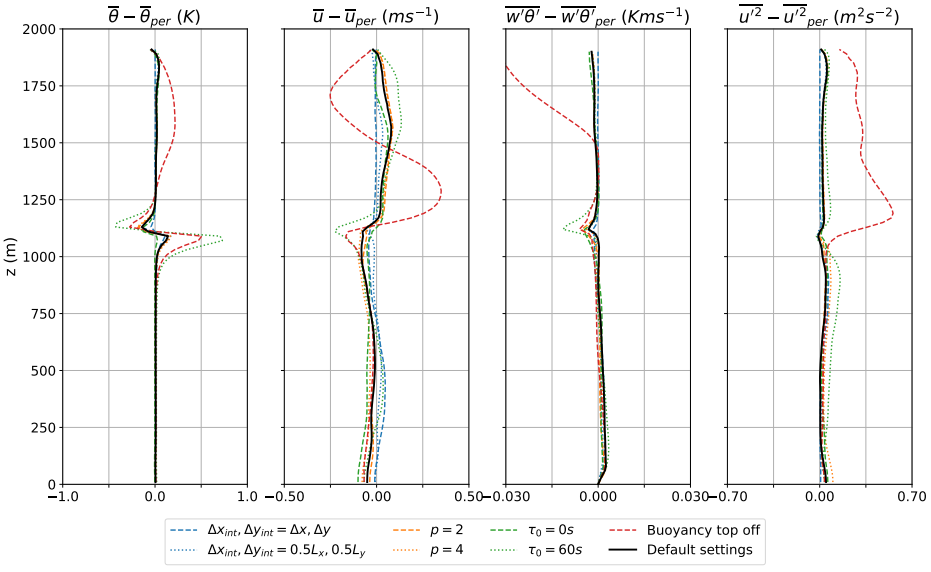

Figure 2. Sensitivity analysis for the open boundary implementation parameters. Slab average profiles for simulations that have parameters perturbed around a default configuration (Table 1). The profiles are calculated over the last half hour of the simulation as a perturbation from the periodic profiles. Left to right; potential temperature, eastward velocity, vertical potential temperature flux, eastward velocity variance.

the chaotic nature of the system. No clear disturbances at any of the boundaries are seen and at the outflow boundary (right) the turbulent fields leave the domain without any significant reflections.

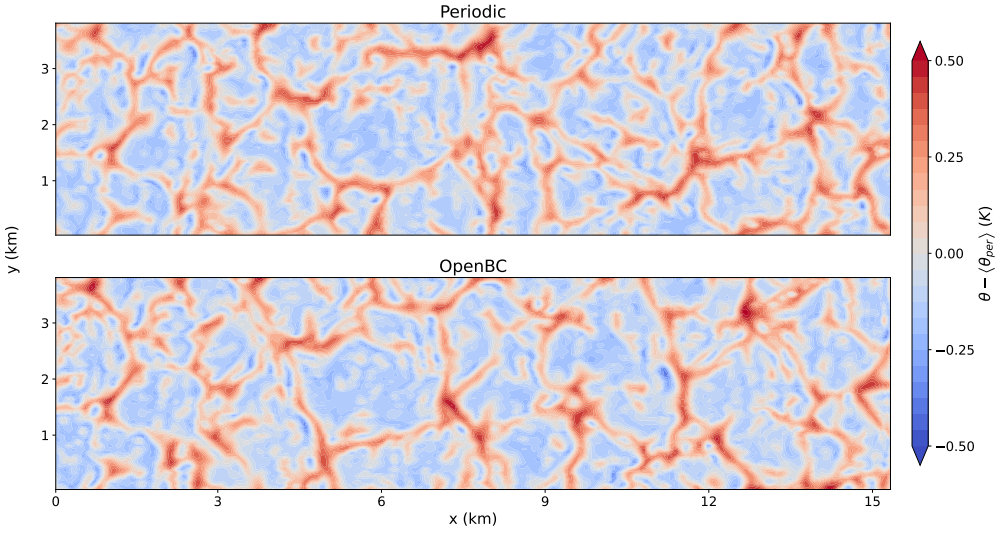

Figure 3. Horizontal cross-section of the potential temperature perturbation with respect to the periodic slab average at a height of 110m for the periodic simulation (top) and open boundary simulation (bottom).

https://doi.org/10.5194/gmd-2023-196
Preprint. Discussion started: 2 November 2023

Geoscientific Model Development Discussions

A more quantitative comparison of the influence of the open boundary conditions on the magnitude of the turbulent perturbations is obtained by comparing turbulent kinetic energy (TKE) cross-sections between the two simulations (Fig. 4). The top panel shows the TKE for the periodic simulation and the bottom panel for the simulation with open boundary conditions after 6 hours of simulation time. The TKE sections are averaged over the last half hour of the simulation and are derived from the velocity perturbations with respect to the cross-wind line averages. The grey dotted (dashed) contour lines mark the areas where the TKE values are smaller (larger) than the 2.5% (97.5%) percentile of the periodic simulation for that height. The black line shows the U/w^* ratio and can be used as a measure of where the information from the surface boundary condition meets the information from the inflow boundary (left). The mean TKE values have similar magnitudes for both simulations. The simulation with open boundary conditions produces larger TKE values above the boundary layer and just before the outflow boundary (right). The increase in TKE above the boundary layer might be caused by the higher wind speeds present in the open boundary simulation (Fig. 2). The increased TKE values at the outflow boundary are the result of reflections and disappears $1\mathrm{km}$ upwind of the outflow boundary.

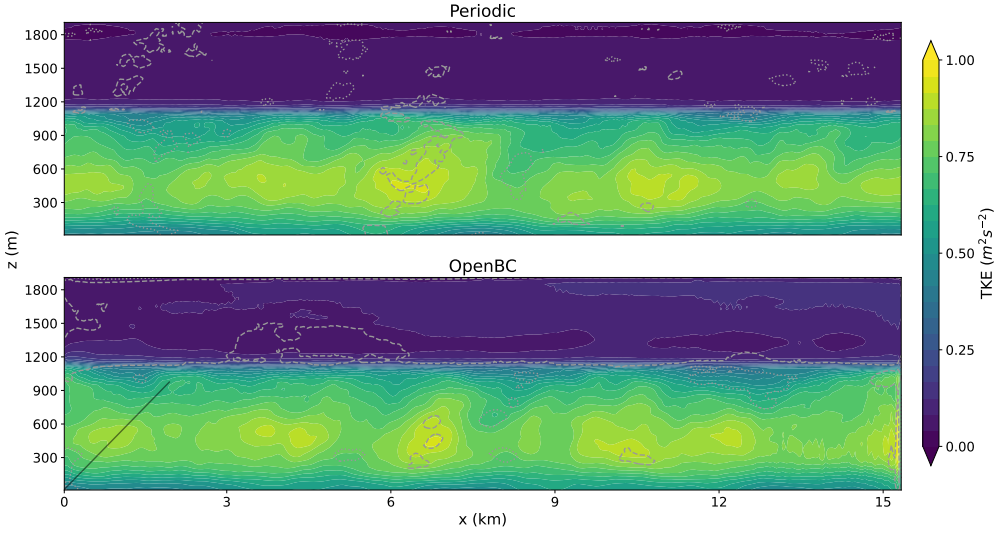

Figure 4. TKE profile derived from the cross-wind direction for the periodic (top) and open boundary (bottom) simulations. The black line indicates the U/w^* ratio. The grey dotted (dashed) contour lines mark the areas where the TKE is smaller (larger) than the 2.5% (97.5%) percentile of the periodic simulation for that height.

A wavelet analysis of the potential temperature field is used to quantify the influence of the open boundary conditions on the power spectrum of the turbulence. Figure 5 shows a wavelet analysis for the periodic (top) and open boundary (bottom) simulations. A one dimensional wavelet analysis is performed in the along-wind direction at $110\mathrm{m}$ after 6 hours of simulation time. The results are averaged over the cross-wind direction. The vertical axis shows the wavelength of the features on a logarithmic axis. The colors denote the wavelet power on a logarithmic scale. The hatched area indicates the combination of wavelengths

https://doi.org/10.5194/gmd-2023-196
Preprint. Discussion started: 2 November 2023

Geoscientific Model Development Discussions

and location for which the analysis window is partly outside of the domain and results within this area should be ignored. The grey dotted (dashed) contour lines mark the areas where the wavelet energy is smaller (larger) than the 2.5% (97.5%) percentile of the periodic simulation for that wavelength. The wavelet analysis shows similar results for both simulations. As expected, least energy is contained in the smallest wavelengths and most energy is contained in features with a wavelength similar to the boundary layer height ($\approx 10^3\mathrm{m}$). There are no clear differences visible between the periodic and open boundary wavelet analysis, which indicates that the open boundary implementation does not influence the turbulent power spectrum.

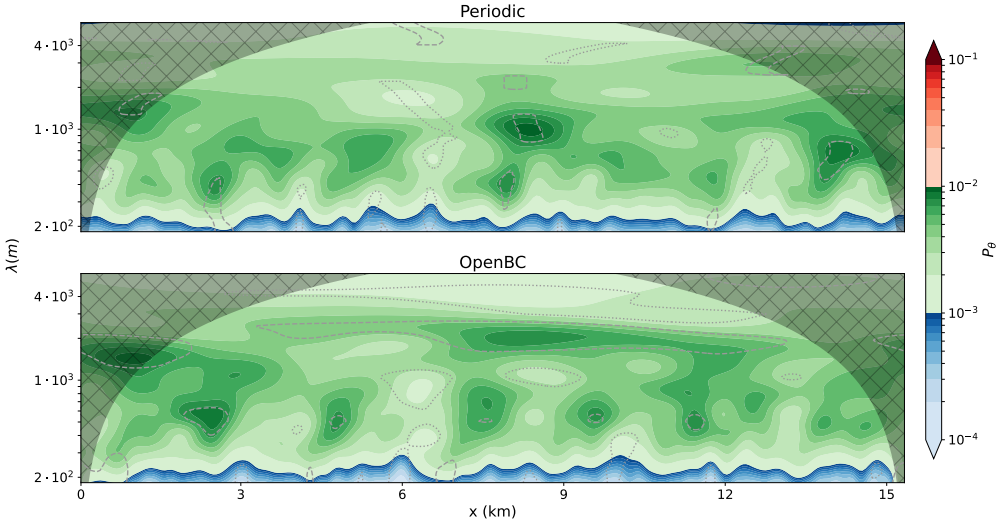

Figure 5. Wavelet analysis of the potential temperature at a height of $110\mathrm{m}$ for the periodic (top) and open boundary (bottom) simulations. The vertical axis shows the wavelengths of the features, the horizontal axis the distance from the inflow boundary and the coloring the energy present. The hatched area is the area where the wavelet window is (partly) outside the domain and should be ignored. The grey dotted (dashed) contour lines mark the areas where the wavelet energy is smaller (larger) than the 2.5% (97.5%) percentile of the periodic simulation for that wavelength.

From Figs. 3-5 it is concluded that the influence of the open boundary implementation on the simulation is minimal. The slab averaged fields, turbulent energy and spectral signature of the simulation are minimally perturbed by the implementation. Furthermore, the results of the sensitivity analysis show that solution is not sensitive to the values of the parameters, as long as they are within a reasonable range and the buoyancy term in the top radiation boundary condition is used.

4.2 Smoothed input simulations

This section will show and discuss the results of the smoothed-input simulations for different degrees of horizontal and temporal smoothing. This setup emulates the situation where the outer model provides boundary fields at a coarser spatial and/or temporal resolution than the LES. The panel in Fig. 6 shows the same cross-section as the bottom panel of Fig. 3 for different degrees of smoothing. The horizontal axis of the panel shows the amount of smoothing in the temporal dimension and the

https://doi.org/10.5194/gmd-2023-196
Preprint. Discussion started: 2 November 2023

Geoscientific Model Development Discussions
Open Access
EGU

vertical axis the amount of smoothing in the horizontal direction. The top left cross-section is the result without smoothing and is the same as the bottom panel of Fig. 3. For low degrees of smoothing, $\sigma_t \leq 30\Delta t$ and $\sigma_x \leq 4\Delta x$, the open boundary simulations resemble the periodic simulation and the solution is not significantly disturbed. For higher degrees of smoothing wavelike structures emerge at the inflow boundary (left) that persist up to $5\mathrm{km}$ into the domain. These structures become more prominent with increased smoohting. Horizontal smoothing (vertical axis) induces features that are aligned in the cross-wind direction. Temporal smoothing result in similar disturbances with the addition of some along-wind disturbances. The spatial-temporal smoothing does not affect the outflow boundary, where turbulent structures leave the domain unperturbed with no visual reflections.

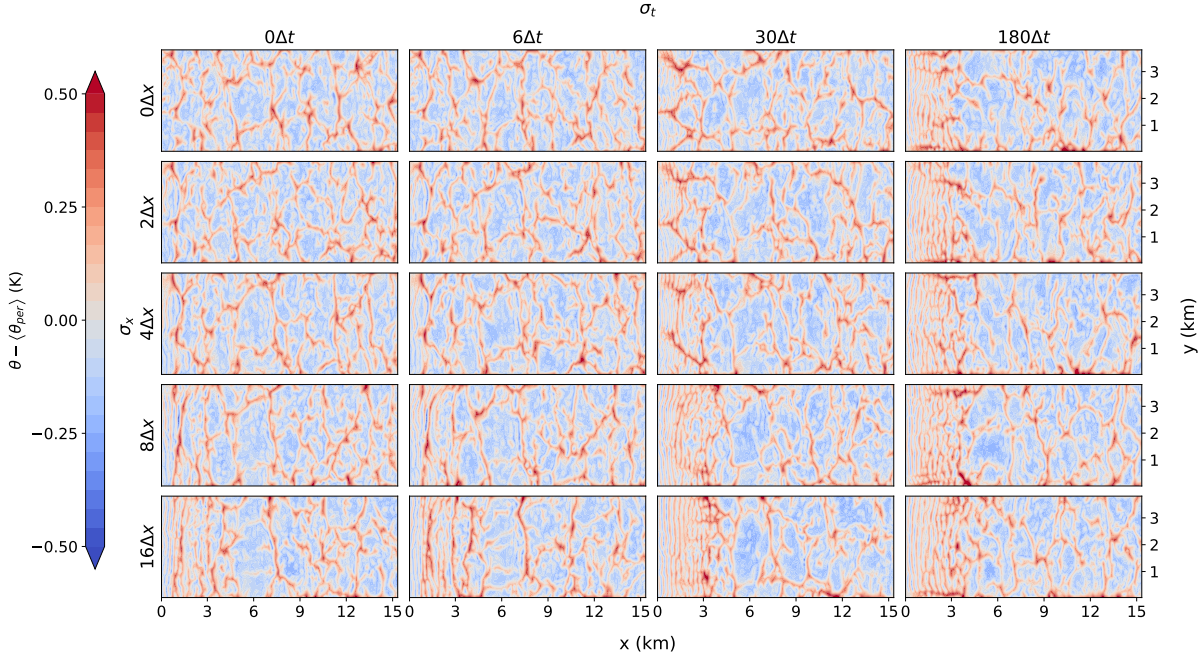

Figure 6. Horizontal cross-section of the potential temperature perturbations with respect to the periodic simulation at a height of $110\mathrm{m}$ (similar to Fig. 3) for different degrees of smoothing. The horizontal axis of the panel shows the amount of smoothing in the temporal dimension and the vertical axis the amount of smoothing in the horizontal direction.

Figure 7 shows the TKE cross-sections for the smoothed-input simulations. Smoothing the input reduces the turbulent scales present in the input data. This results in an area of reduced TKE downwind of the inflow boundary (left). The black line in 7 indicates the ratio between the advective and convective velocity scales (U/w^*). It is expected that upwind (left) of this line the solution will be predominately dominated by information advected from the inflow boundary, whereas downwind (right) of this line convection would take over. The area of reduced TKE values downwind of the inflow boundary increases with increased smoothing and for large degrees of smoothing, the reduced TKE values extent much further than U/w^* ratio. For temporal smoothing of $\sigma_t \geq 30\Delta t$ a burst of TKE is present downwind of the reduced TKE area before settling to a TKE cross-section

https://doi.org/10.5194/gmd-2023-196
Preprint. Discussion started: 2 November 2023

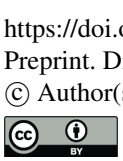

Geoscientific Model Development Discussions

similar to that of the periodic simulation. In the worst cases (highest degrees of smoothing) this can take up to $6-7\mathrm{km}$. The TKE field near the outflow boundary is not affected by the smoothing. The wavelike structures seen in Fig. 6 are not visible in the TKE cross-sections, as they are aligned in the cross-wind direction, the same direction over which the TKE is calculated.

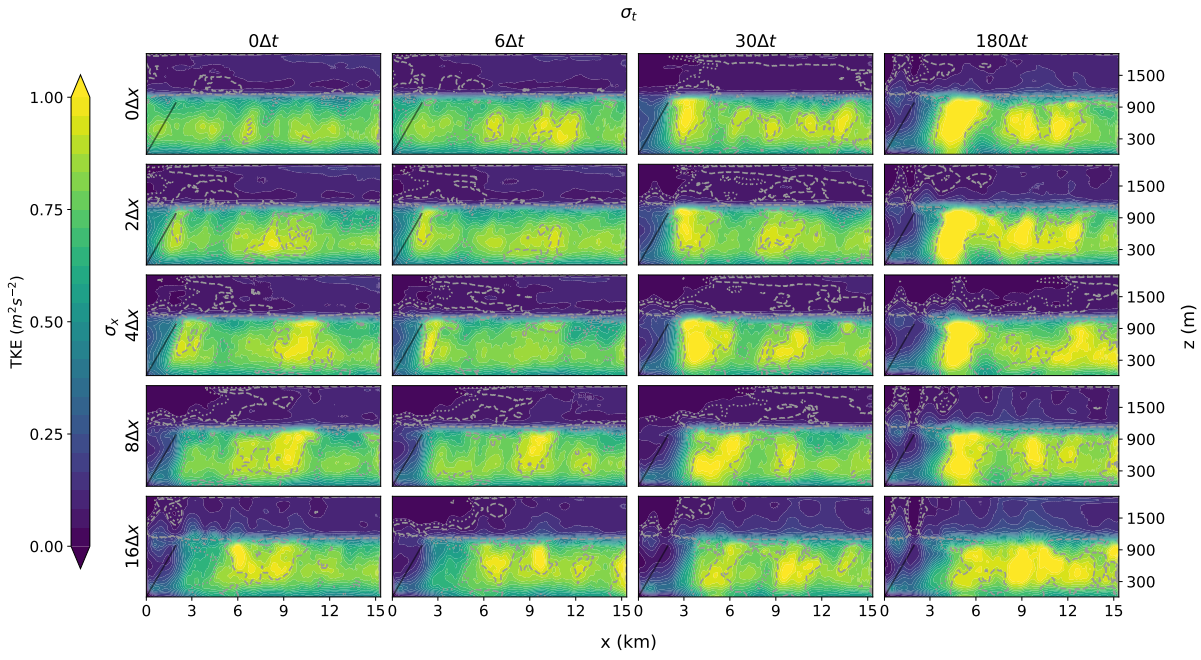

Figure 7. TKE cross-section derived from the cross-wind direction (similar to Fig. 4) for different degrees of smoothing. The horizontal axis of the panel shows the amount of smoothing in the temporal dimension and the vertical axis the amount of smoothing in the horizontal direction.

The wavelet analysis for the smoothed-input simulations is shown in Fig. 8. For low horizontal and temporal smoothing, $\sigma_x \leq 4\Delta x$ and $\sigma_t \leq 30\Delta t$, the influence on the results is small and the wavelet cross-section remains close to the periodic cross-section. For higher degrees of smoothing an increase in energy for wavelengths around $300\mathrm{m}$ is seen at the inflow boundary. The energy increase at these wavelengths represent the waves seen in Fig. 8. The energy increase is larger for increased smoothing. For high degrees of smoothing a decrease in energy is seen for wavelengths around $1\mathrm{km}$ at the inflow boundary. This represents the lack of developed turbulence near the inflow boundary as a result of the missing turbulence in the input data. The energy distribution moves towards the periodic profile downstream from the inflow boundary, with the maximum energy moving towards turbulence of the scale of the boundary layer height. For the highest degrees of smoothing this takes around $7\mathrm{km}$. The smoothing does not influence the wavelet spectrum at the outflow boundary.

The results analysed in Figs. 6-8 show that the input smoothing deteriorates the solution. For high degrees of smoothing, turbulent structures are missing at the inflow boundary and cross-wind oriented wavelike disturbances form. In the worst cases it can take up to $7\mathrm{km}$ before the turbulent intensity and spectral signal evolves towards values close to the results of the periodic

https://doi.org/10.5194/gmd-2023-196
Preprint. Discussion started: 2 November 2023

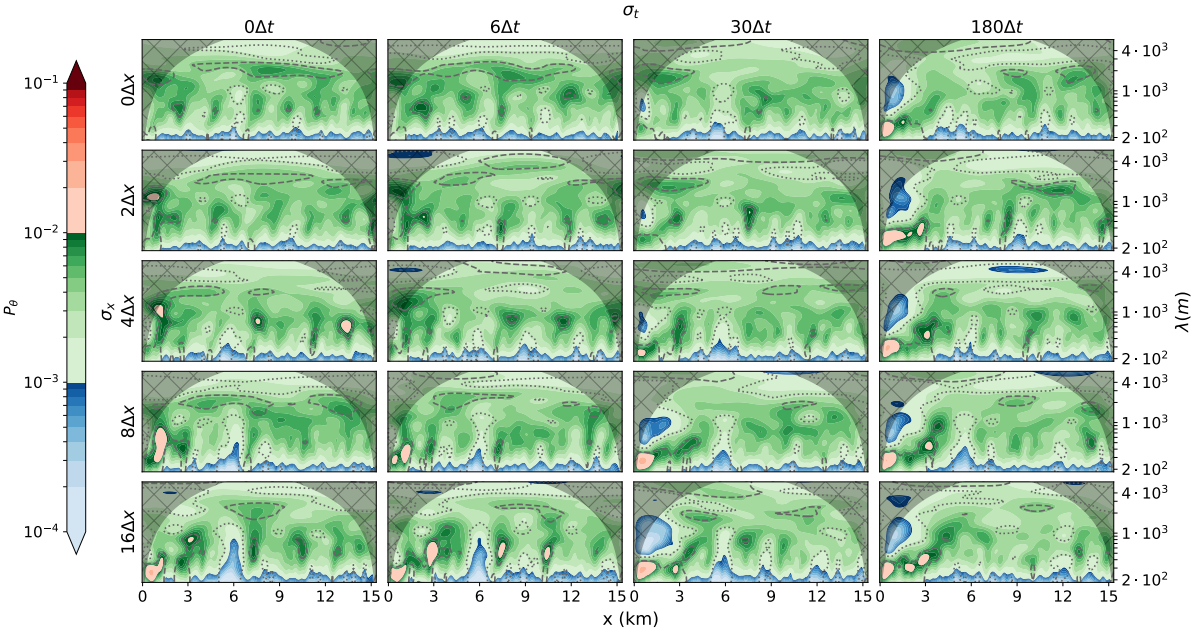

Figure 8. Wavelet analysis of the potential temperature at a height of 110m (similar to Fig. 5) for different degrees of smoothing. The horizontal axis of the panel shows the amount of smoothing in the temporal dimension and the vertical axis the amount of smoothing in the horizontal direction.

simulation. These results are important to take into account when coupling LES models to regional weather models. The latter usually have a spatial resolution on the order of kilometers and common output intervals are on the order of hours. This means that the ratios with the LES gridsize and timestep are at the bottom right of the shown panels. To avoid large ratios between the resolution of the input data and the LES model, repeated nesting can be used. With repeated nesting the LES can step down from the regional weather model resolution towards the desired resolution in steps with a determined refinement ratio. The results in this section suggest that a ratio of 4 between the spatial resolutions and a ratio of 30 between the temporal output and LES timestep should not be exceeded. In practice this is often hard to achieve, especially the temporal constraint as weather model data is often saved on a hourly interval. Another approach is to artificially add finer turbulent scales to the input data. This can be done by turbulence recycling, dedicated turbulence simulations or synthetic turbulence (e.g. Tabor and Ahmadi, 2010).

4.3 Synthetic turbulence simulations

This section will explore the potential of a synthetic turbulence algorithm to mitigate the wave structures found in Sect. 4.2. The algorithm of Smirnov et al. (2001) is implemented and extended to give potential temperature perturbations as well (Sect. 4.3). Figure 9 shows the cross-sections of the potential temperature perturbations with respect to the periodic slab average. Compared to Fig. 6 three things stand out. First, the addition of perturbations seems to remove the wavelike structures at the

https://doi.org/10.5194/gmd-2023-196
Preprint. Discussion started: 2 November 2023

Geoscientific Model Development Discussions
Open Access
EGU

inflow boundary (left). There are still disturbances present, but the wavelike structure is gone. Second, the disturbances seem to disappear more quickly downstream. Third, the disturbances don't increase in magnitude with increased smoothing.

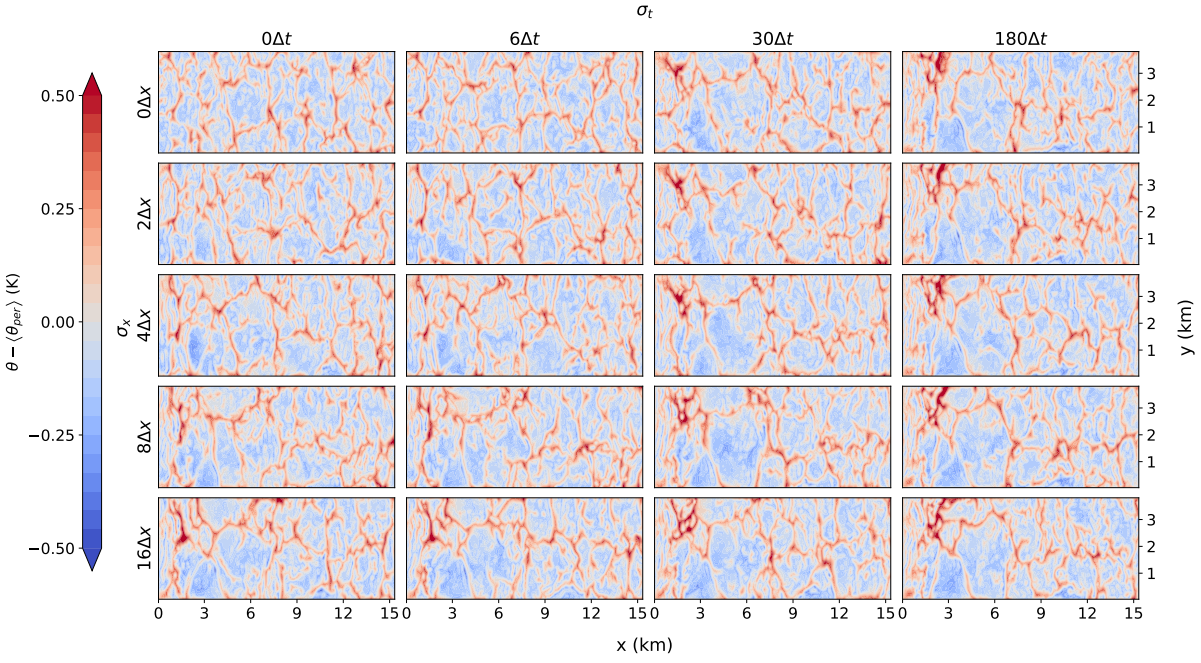

Figure 9. Horizontal cross-section of the potential temperature perturbations with respect to the periodic simulation at a height of $110\mathrm{m}$ for different degrees of smoothing (similar to Fig. 6) with the addition of synthetic turbulence.

Figure 10 shows the TKE cross-sections for the simulations with synthetic turbulence. The addition of synthetic turbulence increases the TKE values directly downstream of the inflow boundary. The values are still below the developed-turbulence values of the periodic simulation. The synthetic turbulence does help to generate developed turbulence faster, which results in a smaller downstream area where the TKE is too low. The overshoot after the reduced TKE is also smaller in magnitude and area compared to Fig. 7. Furthermore, the overshoot no longer increases with increased smoothing in contrast to the results without added synthetic turbulence. The overshoot is similar in shape, magnitude and location for all smoothed simulations and is located near the line that represents the ratio of the convective and advective velocity scales, where the information from the inflow boundary meets with the information from the surface. This means that it can be predicted where the overshoot is and which part of the simulation should be ignored. All simulations settle to a profile close to the periodic simulation within $5\mathrm{km}$ of the inflow boundary. The simulations with high degrees of smoothing do have an area with too much TKE. The addition of synthetic turbulence does not seem to have an influence on the outflow boundary.

Figure 11 shows the wavelet analysis for the smoothed-input open boundary simulations. The increase in energy for wavelengths around $300\mathrm{m}$ is still visible at the inflow boundary, but the magnitude has been reduced by the turbulent perturbations. The decrease in energy for wavelengths around $1\mathrm{km}$ is no longer there. Furthermore, the wavelet profile converges much faster

https://doi.org/10.5194/gmd-2023-196
Preprint. Discussion started: 2 November 2023

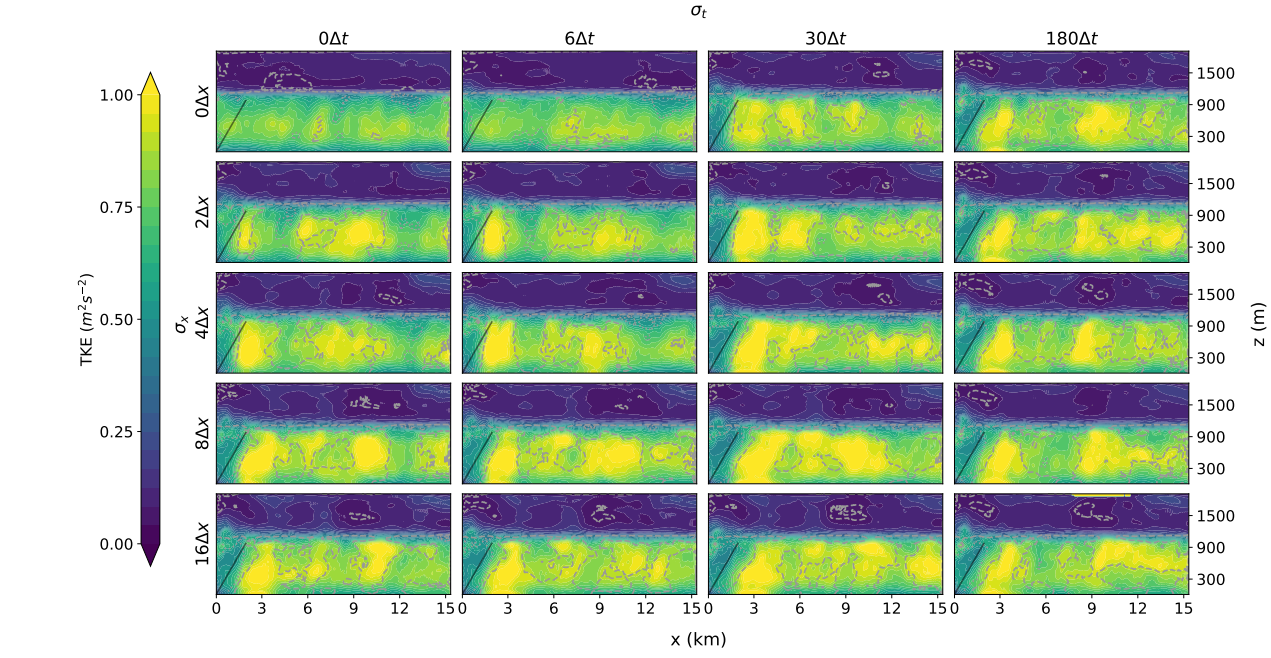

Figure 10. TKE cross-section derived from the cross-wind direction for different degrees of smoothing (similar to Fig. 7) with the addition of synthetic turbulence.

to the periodic profile and the results don't seem to worsen with increased smoothing. The addition of synthetic turbulence does not affect the outflow boundary.

The results analysed in Figs. 9-11 show that the addition of synthetic turbulence on top of coarse input data can improve the simulation results. All of the inflow disturbances found in Sect. 4.2, as a result of coarse input data, were reduced in size and/or magnitude by the addition of synthetic turbulence. Furthermore, the location of the disturbances became predictable and their magnitude and size no longer increased with increased smoothing.

5 Conclusions

This paper introduced an open boundary implementation for atmospheric large eddy simulation models that was implemented in the Dutch Atmospheric Large Eddy Simulation model (DALES). The goal of this research was to give a detailed description of the implementation, investigate it's performance and show the influence of open boundary conditions and boundary input on the solution.

Radiation boundary conditions were implemented as an outflow condition for the boundary-normal velocity components at the lateral and top boundaries. At the top boundary buoyancy was also taken into account, which negated the need to add a sponge layer in the upper parts of the domain. Neumann conditions were used for the other variables at outflow boundaries. For

https://doi.org/10.5194/gmd-2023-196
Preprint. Discussion started: 2 November 2023

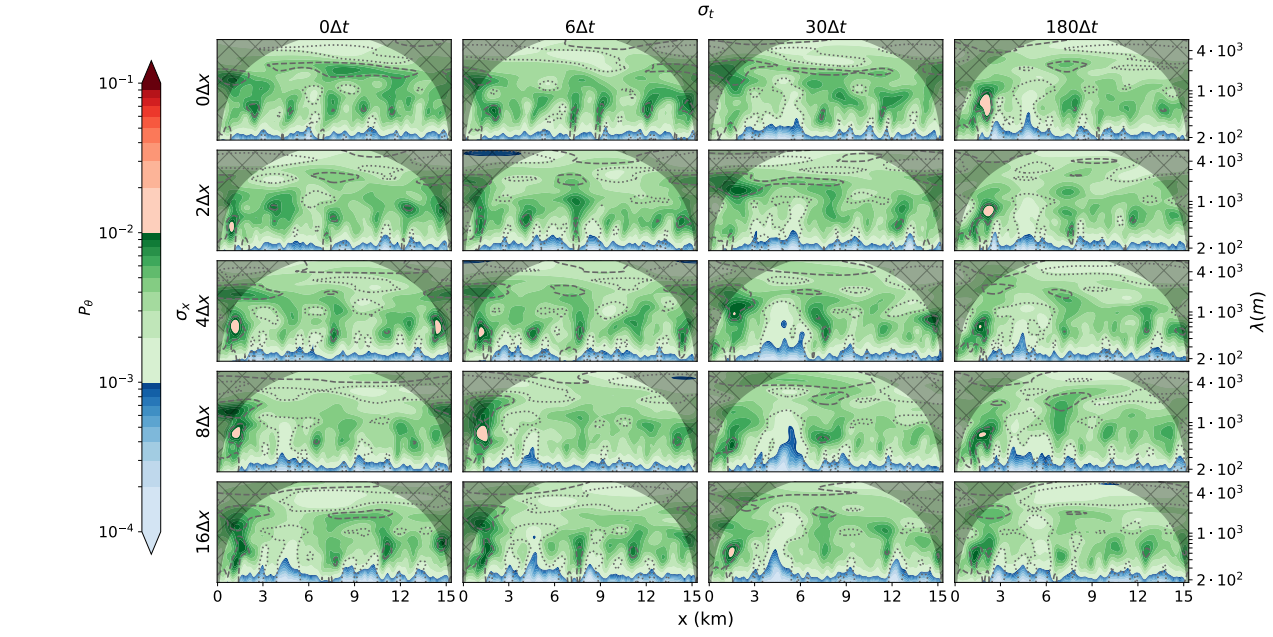

Figure 11. Wavelet analysis of the potential temperature at a height of 110m for different degrees of smoothing (similar to Fig. 8) with the addition of synthetic turbulence.

inflow boundaries a Robin boundary condition was derived for the cell-centered variables and tangential velocity components to allow for a smooth transition between in- and outflow boundaries and a Dirichlet-like condition was implemented for the boundary-normal velocity components.

Using a "Big Brother"-like setup, where a simulation with open boundary conditions was forced by an identical control simulation with periodic boundary conditions on the same spatial and temporal resolution, it was shown that the influence of the boundary implementation on the solution was minimal. Slab averaged profiles showed that the mean profiles are conserved. Furthermore, cross-sections of the potential temperature field showed that the turbulent input data was communicated well through the inflow boundary and that the turbulent fields left the domain without reflections or perturbations at the outflow boundary. Cross-wind turbulent kinetic energy cross-sections showed that the energy in the turbulent perturbations were the same in the simulation with open boundary conditions and the control simulation with periodic boundary conditions. The energy spectrum of the perturbations was also unchanged, which was shown with a wavelet analysis.

To investigate the influence of the spatial and temporal resolution of the input data, the output of the periodic simulation was smoothed before feeding it to the simulation with open boundary conditions. Different degrees of spatial and temporal smoothing showed that a mismatch between input turbulent scales and model scales results in the generation of wavelike disturbances downstream of the inflow boundary. The disturbances grow in size and magnitude when the ratio between input and model scales grows. The lack of turbulence in the input data also results in an area of reduced turbulent kinetic energy downstream of the inflow boundary, where there is no developed turbulence. This area growed as the smoothing increased. For

https://doi.org/10.5194/gmd-2023-196
Preprint. Discussion started: 2 November 2023


Geoscientific Model Development Discussions

large degrees of smoothing it was found that the turbulent energy overshoots before settling to values similar to the periodic control simulation. For these reasons, it is advised to be careful when coupling a large eddy simulation model with open boundary conditions to a coarser model. Repeated nesting can be used and is currently being explored to step down in multiple steps from coarse data to the desired resolution. The results of this research indicate that the refinement factor when nesting should not exceed 4 in the spatial dimension and 30 in the time dimension.

The potential of adding synthetic turbulence to the LBCs was explored and the results show that it can help to reduce the found disturbances in size and magnitude and to speed up the process of obtaining developed turbulence by artificially reducing the gap between the input turbulent scales and model scales. The strong wavelike character of the disturbances were removed and the length of the inflow area required for turbulence to develop was reduced. The disturbances and development area also became less dependent on the degree of smoothing and the development area is given by the ratio of the advective and convective velocity scales. However, if possible, we would still advise to keep the spatial and temporal ratios between the input data and the LES below the earlier mentioned values.

Code and data availability. The current version of DALES is available from the project website: https://github.com/dalesteam/dales under the GNU General Public License. The exact version of the model used to produce the results used in this paper is archived on Zenodo, as are input data and scripts to run the model and produce the plots for all the simulations presented in this paper (Liqui Lung et al., 2023).

Author contributions. FLL conceptualized the paper, did the formal analysis and visualization, implemented the methodology and software and wrote and edited the draft. CJ and PS supervised during the project, reviewed the draft and supported in the conceptualization. FJ supported the software implementation and reviewed the draft.

Competing interests. The authors declare that there are no competing interests

Acknowledgements. We acknowledge the use of ECMWF's computing and archive facilities, the funding provided by the Australian Research Council Centre of Excellence for Climate Extremes (CE170100023) and the support of the Ruisdael Observatory, a scientific research infrastructure which is (partly) financed by the Dutch Research Council (NWO, grant number 184.034.015)

https://doi.org/10.5194/gmd-2023-196
Preprint. Discussion started: 2 November 2023

References

Craske, J. and Van Reeuwijk, M.: Robust and accurate open boundary conditions for incompressible turbulent jets and plumes, Comput. Fluids, 86, 284–297, https://doi.org/10.1016/j.compfluid.2013.06.026, 2013.

Deardorff, J.: Numerical Investigation of Neutral and Unstable Planetary Boundary Layers, J. Atmos. Sci., 29, 91–115, https://doi.org/10.1175/1520-0469(1972)029<0091:NIONAU>2.0.CO;2, 1972.

Denis, B., Laprise, R., Caya, D., and Côté, J.: Downscaling ability of one-way nested regional climate models: The Big-Brother Experiment, Clim. Dynam., 18, 627–646, https://doi.org/10.1007/s00382-001-0201-0, 2002.

Giometto, M., Christen, A., Meneveau, C., Fang, J., Krafczyk, M., and Parlange, M.: Spatial Characteristics of Roughness Sublayer Mean Flow and Turbulence Over a Realistic Urban Surface, Bound.-Lay. Meteorol., 160, 425–452, https://doi.org/10.1007/s10546-016-0157-6, 2016.

Hedley, M. and Yau, M.: Radiation Boundary Conditions in Numerical Modeling, Mon. Weather Rev., 116, 1721–1736, https://doi.org/10.1175/1520-0493(1988)116<1721:RBCINM>2.0.CO;2, 1988.

Heinze, R., Dipankar, A., Henken, C. C., Moseley, C., Sourdeval, O., Trömel, S., Xie, X., Adamidis, P., Ament, F., Baars, H., Barthlott, C., Behrendt, A., Blahak, U., Bley, S., Brdar, S., Brueck, M., Crewell, S., Deneke, H., Di Girolamo, P., Evaristo, R., Fischer, J., Frank, C., Friederichs, P., Göcke, T., Gorges, K., Hande, L., Hanke, M., Hansen, A., Hege, H.-C., Hoose, C., Jahns, T., Kalthoff, N., Klocke, D., Kneifel, S., Knippertz, P., Kuhn, A., van Laar, T., Macke, A., Maurer, V., Mayer, B., Meyer, C. I., Muppa, S. K., Neggers, R. A. J., Orlandi, E., Pantillon, F., Pospichal, B., Röber, N., Scheck, L., Seifert, A., Seifert, P., Senf, F., Siligam, P., Simmer, C., Steinke, S., Stevens, B., Wapler, K., Weniger, M., Wulfmeyer, V., Zängl, G., Zhang, D., and Quaas, J.: Large-eddy simulations over Germany using ICON: a comprehensive evaluation, Q. J. Roy. Meteor. Soc., 143, 69–100, https://doi.org/10.1002/qj.2947, 2017.

Heus, T., van Heerwaarden, C., Jonker, H., Siebesma, A., Axelsen, S., Dries, K., Geoffroy, O., Moene, A., Pino Gonzalez, D., Roode, S., and Arellano, J.: Formulation of the Dutch Atmospheric Large-Eddy Simulation (DALES) and overview of its applications, Geosci. Model Dev., 3, 415–444, https://doi.org/10.5194/gmd-3-415-2010, 2010.

Huang, S., Li, Q., and Wu, J.: A general inflow turbulence generator for large eddy simulation, J. Wind Eng. Ind. Aerod., 98, 600–617, https://doi.org/10.1016/j.jweia.2010.06.002, 2010.

Kadasch, E., Sühring, M., Gronemeier, T., and Raasch, S.: Mesoscale nesting interface of the PALM model system 6.0, Geosci. Model Dev., 14, 5435–5465, https://doi.org/10.5194/gmd-14-5435-2021, 2021.

Klemp, J. and Wilhelmson, R.: The Simulation of Three-Dimensional Convective Storm Dynamics, J. Atmos. Sci., 35, 1070–1096, https://doi.org/10.1175/1520-0469(1978)035<1070:TSOTDC>2.0.CO;2, 1978.

Kurppa, M., Hellsten, A., Auvinen, M., Raasch, S., Vesala, T., and Järvi, L.: Ventilation and Air Quality in City Blocks Using Large-Eddy Simulation—Urban Planning Perspective, Atmosphere-Basel, 9, 65, https://doi.org/10.3390/atmos9020065, 2018.

Lac, C., Chaboureau, J.-P., Masson, V., Pinty, J.-P., Tulet, P., Escobar, J., Leriche, M., Barthe, C., Aouizerats, B., Augros, C., Aumond, P., Auguste, F., Bechtold, P., Berthet, S., Bielli, S., Bosseur, F., Caumont, O., Cohard, J.-M., Colin, J., Couvreux, F., Cuxart, J., Delautier, G., Dauhut, T., Ducrocq, V., Filippi, J.-B., Gazen, D., Geoffroy, O., Gheusi, F., Honnert, R., Lafore, J.-P., Lebeaupin Brossier, C., Libois, Q., Lunet, T., Mari, C., Maric, T., Mascart, P., Mogé, M., Molinié, G., Nuissier, O., Pantillon, F., Peyrillé, P., Pergaud, J., Perraud, E., Pianezze, J., Redelsperger, J.-L., Ricard, D., Richard, E., Riette, S., Rodier, Q., Schoetter, R., Seyfried, L., Stein, J., Suhre, K., Taufour, M., Thouron, O., Turner, S., Verrelle, A., Vié, B., Visentin, F., Vionnet, V., and Wautelet, P.: Overview of the Meso-NH model version 5.4 and its applications, Geosci. Model Dev., 11, 1929–1969, https://doi.org/10.5194/gmd-11-1929-2018, 2018.

https://doi.org/10.5194/gmd-2023-196
Preprint. Discussion started: 2 November 2023

Lafore, J.-P., Stein, J., Asencio, N., Bougeault, P., Ducrocq, V., Duron, J., Fischer, C., Héreil, P., Mascart, P., Masson, V., Pinty, J.-P., Redelsperger, J.-L., Richard, E., and Arellano, J.: The Meso-NH Atmospheric Simulation System. Part I: Adiabatic formulation and control simulations, Ann. Geophys., 16, 90–109, https://doi.org/10.1007/s005850050582, 1998.

Lilly, D.: The presentation of small-scale turbulence in numerical simulation experiments, 281, National Center for Atmospheric Research: Boulder, CO, USA, https://doi.org/10.5065/D62R3PMM, also featured in Proc. IBM Sci. Comput. Symp. on Environmental Science 1967 (pp. 195-210), 1966.

Liqui Lung, F. P. A., Siebesma, A. P., Jansson, F. R., Arabas, S., Axelsen, S. L., Attema, J., Azizi, V., Beets, C., Boeing, S. J., de Bruine, M., Chylik, J., Cuijpers, H., van Dorp, P., van der Dussen, J., Duynkerke, P., van Heerwaarden, C., Heus, T., Janssens, M., Jonker, H., Moene, A., Nieuwstadt, F., Ouwersloot, H., van den Oord, G., Pourquie, M., de Roode, S., Neggers, R., Pedruzo, X., Sikma, M., van Stratum, B., Vila, J., and van Zanten, M.: franslql/dales: DALES 4.4 with open boundary conditions, (v4.4_openBC). Zenodo. https://doi.org/10.5281/zenodo.10046420, 2023.

Maronga, B., Gryschka, M., Heinze, R., Hoffmann, F., Kanani-Sühring, F., Keck, M., Ketelsen, K., Letzel, M. O., Sühring, M., and Raasch, S.: The Parallelized Large-Eddy Simulation Model (PALM) version 4.0 for atmospheric and oceanic flows: model formulation, recent developments, and future perspectives, Geosci. Model Dev., 8, 2515–2551, https://doi.org/10.5194/gmd-8-2515-2015, 2015.

Maronga, B., Banzhaf, S., Burmeister, C., Esch, T., Forkel, R., Fröhlich, D., Fuka, V., Gehrke, K. F., Geletič, J., Giersch, S., Gronemeier, T., Groß, G., Heldens, W., Hellsten, A., Hoffmann, F., Inagaki, A., Kadasch, E., Kanani-Sühring, F., Ketelsen, K., Khan, B. A., Knigge, C., Knoop, H., Krč, P., Kurppa, M., Maamari, H., Matzarakis, A., Mauder, M., Pallasch, M., Pavlik, D., Pfafferott, J., Resler, J., Rissmann, S., Russo, E., Salim, M., Schrempf, M., Schwenkel, J., Seckmeyer, G., Schubert, S., Sühring, M., von Tils, R., Vollmer, L., Ward, S., Witha, B., Wurps, H., Zeidler, J., and Raasch, S.: Overview of the PALM model system 6.0, Geosci. Model Dev., 13, 1335–1372, https://doi.org/10.5194/gmd-13-1335-2020, 2020.

Mazzaro, L., Muñoz-Esparza, D., Lundquist, J., and Linn, R.: Nested mesoscale-to-LES modeling of the atmospheric boundary layer in the presence of under-resolved convective structures, J. Adv. Model. Earth Sy., 9, 1795–1810, https://doi.org/10.1002/2017MS000912, 2017.

Mehta, D., Zuijlen, A., Koren, B., Holierhoek, J., and Bijl, H.: Large Eddy Simulation of wind farm aerodynamics: A review, J. Wind Eng. Ind. Aerod., 133, 1–17, https://doi.org/10.1016/j.jweia.2014.07.002, 2014.

Moeng, C.-H., Dudhia, J., Klemp, J., and Sullivan, P.: Examining Two-Way Grid Nesting for Large Eddy Simulation of the PBL Using the WRF Model, Mon. Weather Rev., 135, 2295–2311, https://doi.org/10.1175/MWR3406.1, 2007.

Muñoz-Esparza, D., Kosovic, B., Mirocha, J., and Beeck, J.: Bridging the Transition from Mesoscale to Microscale Turbulence in Numerical Weather Prediction Models, Bound.-Lay. Meteorol., 153, 409–440, https://doi.org/10.1007/s10546-014-9956-9, 2014.

Muñoz-Esparza, D., Kosović, B., van Beeck, J., and Mirocha, J.: A stochastic perturbation method to generate inflow turbulence in large-eddy simulation models: Application to neutrally stratified atmospheric boundary layers, Phys. Fluids, 27, https://doi.org/10.1063/1.4913572, 035102, 2015.

Ol'shanskii, M. A. and Staroverov, V. M.: On simulation of outflow boundary conditions in finite difference calculations for incompressible fluid, Int. J. Numer. Meth. Fl., 33, 499–534, https://doi.org/10.1002/1097-0363(20000630)33:4<499::AID-FLD19>3.0.CO;2-7, 2000.

Orlanski, I.: Simple boundary condition for unbounded flows, J. Comput. Phys., 21, 251–269, https://doi.org/10.1016/0021-9991(76)90023-1, 1976.

Sani, R. and Gresho, P.: Résumé and remarks on the Open Boundary Condition Minisymposium, Int. J. Numer. Meth. Fl., 18, 983–1008, https://doi.org/10.1002/fld.1650181006, 1994.

https://doi.org/10.5194/gmd-2023-196
Preprint. Discussion started: 2 November 2023

Schalkwijk, J., Jonker, H., Siebesma, A., and Meijgaard, E.: Weather Forecasting Using GPU-Based Large-Eddy Simulations, B. Am. Meteorol. Soc., 96, 715–723, https://doi.org/10.1175/BAMS-D-14-00114.1, 2015.

Skamarock, W. C., Klemp, J. B., Dudhia, J., Gill, D. O., Liu, Z., Berner, J., Wang, W., Powers, J. G., Duda, M. G., Barker, D., and Huang, X.: A Description of the Advanced Research WRF Model Version 4.3, Tech. Rep. NCAR/TN-556+STR, National Center for Atmospheric Research: Boulder, CO, USA, https://doi.org/10.5065/1dfh-6p97, 2021.

Smirnov, A., Shi, S., and Celik, I.: Random Flow Generation Technique for Large Eddy Simulations and Particle-Dynamics Modeling, J. Fluid. Eng.-T. ASME, 123, 359–371, https://doi.org/10.1115/1.1369598, 2001.

Sommerfeld, A.: Partial differential equations in physics, Academic press, https://doi.org/10.1016/B978-0-12-654658-3.X5001-0, 1949.

Sommeria, G.: Three-Dimensional Simulation of Turbulent Processes in an Undisturbed Trade Wind Boundary Layer, J. Atmos. Sci., 33, 216–241, https://doi.org/10.1175/1520-0469(1976)033<0216:TDSOTP>2.0.CO;2, 1976.

Tabor, G. and Ahmadi, M.: Inlet conditions for large eddy simulation: A review, Comput. Fluids, 39, 553–567, https://doi.org/10.1016/j.compfluid.2009.10.007, 2010.

Talbot, C., Bou-Zeid, E., and Smith, J.: Nested Mesoscale Large-Eddy Simulations with WRF: Performance in Real Test Cases, J. Hydrometeorol., 13, 1421–1441, https://doi.org/10.1175/JHM-D-11-048.1, 2012.

Wesseling, P.: Principles of computational fluid dynamics, vol. 29, Springer Science & Business Media, https://doi.org/10.1007/978-3-642-05146-3, 2009.

Zhu, P., Albrecht, B., Ghate, V., and Zhu, Z.: Multiple-scale simulations of stratocumulus clouds, J. Geophys. Res., 115, https://doi.org/10.1029/2010JD014400, 2010.